Tip-Assisted Raman Thermal Probing and Nanoscale Trapping

Hongkai Zhang[1,2†], Dezhao Huang[1,2†*], Xiaona Huang[1,2], Nan Zhang[1,2], Shijing Wu[1,2], Jarrod E. Schiffbauer[3], Sheng Liu[1], and Yanan Yue[4*]

[1]*School of Power and Mechanical Engineering, Wuhan University, Wuhan 430072, China*
[2]*Institute for Goneo New Energy, Wuhan University, Wuhan 430072, China*
[3]*Department of Physical and Environmental Sciences, Colorado Mesa University, Colorado 81501, United States of America*
[4]*Department of Mechanical and Manufacturing Engineering, Miami University, Ohio 45056, United States of America*

(Received 16 May 2025; accepted manuscript online 4 July 2025)

Precise control and measurement of nanoparticles using low-power optical tweezers are pivotal for advancing single-particle analysis, nanoscale sensing, and energy transport research. In this work, we present the tip-assisted nanoparticle capture system that simultaneously achieves localized temperature probing and nanoparticle trapping, significantly lowering the required laser power input. Unlike traditional metal-tip plasmonic techniques that predominantly rely on intense electric field gradients, our approach employs a silicon nanotip under resonant laser excitation, uniquely integrating optical forces, thermophoretic forces, and interatomic interactions for stable nanoparticle confinement. This synergistic collaboration mechanism enables approximately a 42% reduction in laser power density compared to conventional bowtie nanoaperture methods. This experimental method achieved direct and simultaneous Raman-based measurements of localized thermal dynamics, providing new insights into nanoscale thermodynamics during optical trapping. Additionally, the silicon nanotip demonstrates reduced thermal transport due to its confined nanoscale geometry, aligning closely with our theoretical predictions. Our integrated strategy of efficient nanoparticle manipulation coupled with precise thermal probing not only enhances overall energy efficiency but also broadens the scope of potential applications in cutting-edge nanoscience and nanotechnology.

DOI: 10.1088/0256-307X/42/8/080801 CSTR: 32039.14.0256-307X.42.8.080801

1. Introduction. Optical tweezers, which utilize focused laser beams to exert forces on particles, have found widespread applications in various scientific disciplines,[1–3] including biology,[4–6] nanotechnology,[7–9] and physics.[10–12] However, the traditional operation of optical tweezers often involves high-power laser sources, which can induce photodamage to biological specimens and may alter the properties of delicate nanostructures.[13,14] This underscores the critical need for developing low-power optical tweezers, which promise to mitigate these adverse effects yet maintain the capability for precise trapping. Nonetheless, the transition to low-power systems is fraught with challenges. Key among these is optimizing trap efficiency and stability, which are compromised at reduced power levels because of decreased gradient forces.[15] For instance, Hansen *et al.*[16] have established stable three-dimensional (3D) optical trapping of gold nanoparticles (Au NPs) with sizes from 18–254 nm using a single laser beam that required a considerable amount of laser power ranging from 135–900 mW.

Current advancements[17–19] have underscored the effectiveness of plasmonic optical tweezers (POTs), which combine plasmonic effects with the principles of optical tweezing, in substantially reducing the power required for trapping particles. By enhancing the intensity and gradient of the local electromagnetic field near plasmonic structures, such as atomic force microscopy (AFM) tips and nanoarrays, POTs have demonstrated their capability to achieve this reduction. Novotny *et al.*[20] developed a model for trapping dielectric spheres with a diameter of 10 nm using a gold probe. This model utilizes the electric field gradient close to the probe's apex to trap dielectric particles when exposed to laser light, maintaining a safe power level of 65 $\mathrm{mW\cdot\mu m^{-2}}$. This approach not only reduces the need for high laser intensity but also diminishes the risk of heat-induced damage to the trapped particles. Mestres[21] subsequently developed bowtie nanoapertures that could trap 60 nm Au NPs with substantially lower incident powers of 0.26 $\mathrm{mW\cdot\mu m^{-2}}$. This advancement further highlights the potential of POTs to markedly reduce the laser power necessary for particle trapping, presenting a promising avenue for minimizing energy consumption and preventing damage in optical trapping applications.

In this study, we developed a tip-assisted nanoparti-

†These authors contributed equally to this work.
*Corresponding authors. Email: dhuang2@whu.edu.cn; yyue@miamioh.edu
© 2025 Chinese Physical Society and IOP Publishing Ltd. All rights, including for text and data mining, AI training, and similar technologies, are reserved.

cle capture system that can not only enable the trapping of nanoparticles at substantially lower laser powers but also provide real-time, localized temperature measurements. We experimentally and computationally confirmed the strong single-beam optical trapping potential of Au NPs in the vicinity of the nanotip at a minimal laser power density of $0.15\,\mathrm{mW{\cdot}\mu m^{-2}}$. Our observations indicate that Au NPs remain attached to the tip surface post experimentation. Furthermore, we conducted an analysis of the local thermal conductivity at the nanotip and evaluated the plasmonic heating effects on both the tip as well as Au NPs through a combination of Raman thermometry and finite-element simulations. Our findings have substantial implications for enhancing plasmonic optical trapping technology at reduced power levels.

2. Experimental Section/Methods.

2.1. Calculation of Optical Forces and Heat. Finite element method (FEM) is performed to analyze the distribution of electromagnetic and temperature fields by coupling multiple physical interfaces: the heat transfer module and electromagnetic wave frequency domain (EWFD) module. The research type is set as frequency domain for the EWFD module and steady state for the heat transfer module. In the construction of geometric models, the silicon nanotip is simplified to a 3D cone model, which features a height of 500 nm, a half angle of $\theta = 20^\circ$, and a curvature radius of $r_1 = 6\,\mathrm{nm}$. Note that r_1 in the FEM model is set to 6 nm unless otherwise specified in this work. The computational region is a $1500\times1000\times1000\,\mathrm{nm^3}$ rectangular volume, which is enclosed by a perfect matching layer with a thickness of 100 nm to absorb excess light sources from boundary scattering.

In the EWFD module, a paraxial approximate Gaussian beam is directed vertically onto the tip, in which the detailed laser parameters are consistent with the experimental setup. The laser wavelength is determined by the frequency domain in the research, which is set at 532 nm. The electric displacement field model selects the refractive index for calculation. The complex refractive indices of water, silicon tip, and Au NP at the corresponding wavelength are 1.33, 4.15 + 0.052i, and 0.54 + 2.23i, respectively. To conduct heat conduction simulation, the thermal conductivities of water and Au NPs are $0.58\,\mathrm{W{\cdot}m^{-1}{\cdot}K^{-1}}$ and $314\,\mathrm{W{\cdot}m^{-1}{\cdot}K^{-1}}$, respectively. The thermal conductivity of the silicon tip is determined by the local thermal conductivity method proposed by Chen.[22] The boundary temperature of the surrounding medium is set as room temperature (293.15 K). The heat sources generated inside the silicon nanotip are determined by electromagnetic losses from the EWFD module,

$$\boldsymbol{F}_\mathrm{o} = \iint \boldsymbol{T}\cdot\boldsymbol{n}\mathrm{d}s\,, \tag{1}$$

where $\boldsymbol{n}$ is the unit normal vector of the surface; and $\boldsymbol{T}$ is the time-averaged Maxwell stress tensor, which can be written as[23,24]

$$\boldsymbol{T} = \frac{1}{2}\mathrm{Re}\Big[\varepsilon\boldsymbol{E}\boldsymbol{E}^* + \mu\boldsymbol{H}\boldsymbol{H}^* - \frac{\boldsymbol{I}}{2}(\varepsilon\boldsymbol{E}\cdot\boldsymbol{E}^* + \mu\boldsymbol{H}\cdot\boldsymbol{H}^*)\Big], \tag{2}$$

where $\boldsymbol{I}$ represents the unit tensor, ε is the dielectric constant of water, μ is the magnetic permeability of water, and * is the conjugate complex.

2.2. Capture Experiment. A colloidal solution (0.02 g/mL, 60 nm, Xianfeng Nano) was subjected to ultrasonic treatment for 3 minutes to ensure uniform dispersion of Au NPs prior to trapping experiments. Subsequently, 0.5 mL of the colloidal solution was dispensed into a quartz dish, at the bottom of which an AFM tip (Scansens, CSG01 series, curvature radius 6–10 nm) was positioned. During the capture experiment, a continuous-wave laser with a center wavelength of 532 nm was employed, operating at a fixed power of 6.4 mW. A 20× objective lens was used to focus the laser in a manner that achieved a spot radius of 3.7 μm, measured using the knife-edge method. The scattered light was collected back through the objective lens and an optical filter, then directed onto the sensor of a high-speed complementary metal-oxide-semiconductor camera. The position of the laser focus and the tip was observed in the camera, and the tip was aligned with the laser focus using a translation stage. It is noted that the polarization direction of the laser is consistent with the extension direction of the tip during trapping.

2.3. Raman Thermal Probing. The localized temperature of the silicon tip was determined via temperature-dependent Raman spectroscopy, a non-contact technique renowned for its high spatial resolution.[25–27] However, thermal stress induced by the tip under laser irradiation will introduce shifts in Raman peaks,[28,29] leading to inaccuracies in Raman-shift-based thermometry. While the full width at half-maximum (FWHM) of Raman peaks broadens with increasing temperature due to reduced phonon lifetime, it is notably insensitive to thermal stress.[28] Consequently, FWHM was selected as the primary parameter for localized temperature measurement. Near room temperature, FWHM usually exhibits a nearly linear dependence on temperature, but higher-temperature regimes require consideration of higher-order anharmonicity effects. The relationship between FWHM and temperature increments can be expressed as follows:

$$\Gamma = B\Delta T^2 + C\Delta T + \Gamma_0\,, \tag{3}$$

where Γ is FWHM, B and C are calibrated parameters, ΔT indicates the temperature increases relative to room temperature, and Γ_0 is FWHM at room temperature. Usually, these parameters can be obtained through a solo calibration experiment. At last, tip's temperatures are determined at various laser power levels by combining the power-FWHM relation obtained from the experiment.

2.4. Interatomic Interactions Based on Molecular Dynamics Simulation. In this Letter, to validate our findings, we conducted a more realistic simulation using large-scale atomic/molecular massively parallel simulator, where the water molecules were modeled by the SPC/E model,[30] which is known for providing accurate dynamics and structure for bulk water. The non-bond interactions between Au atoms and water molecules were simulated using the L–J interaction.[31–33] For the Au NP, we employed the

Morse potential[34] with a force cutoff threshold of 8 Å, while the L–J interactions were applied within a cutoff of 12 Å. In the molecular dynamics simulations, the Morse potential is

$$E(r) = D_0 \left[e^{-2\alpha(r-r_0)} - 2e^{-\alpha(r-r_0)} \right], \quad (4)$$

where D_0 is the bond-dissociation energy, r_0 is the equilibrium bond length, and α is the parameter characteristic of the atom. This potential is used to simulate the interactions among Au atoms and the bond interaction between the Au substrate and the sulfur (S) atoms in the thiol self-assembled monolayer molecules. Such a potential has been previously used for self-assembled monolayer on Au structures successfully.[33,35,36]

The non-bonded interactions between Au and other atoms are simulated by the Lennard–Jones interaction,

$$E = 4\varepsilon \left[\left(\frac{\sigma}{r_{ij}} \right)^{12} - \left(\frac{\sigma}{r_{ij}} \right)^{6} \right], \quad (5)$$

where ε and σ are the representative scales of energy and length, r_{ij} is the distance between two molecules i and j. L–J interaction parameters are chosen from a modified universal force field.[37,38] To account for the long-range electrostatic interactions within the system, we employed the particle-particle particle-mesh method, characterized by an accuracy of 10^{-5}. During these simulations, we adopted a timestep of 1 femtosecond. The simulation process began with energy minimization and equilibration in an NVT ensemble at 300 K for 1 ns. Subsequently, the system underwent optimization in an NPT ensemble at 1 atm and 300 K for an additional 1 ns. Once the system was fully relaxed, the NP (diameter = 60 nm) was released to observe the normal Brownian motion phenomenon.

3. Results and Discussion.

3.1. Induced Directional Optical Force. Our study begins with a force analysis on the Au NPs near the tip to evaluate its capability for trapping these particles under continuous-wave laser illumination at a wavelength of 532 nm, matching the surface plasmon resonance of the apex and Au NPs. For Rayleigh-sized Au NPs, previous studies have indicated that forces due to both radiation pressure, i.e., a scattering force, and a force proportional to the gradient of optical intensity due to the polarizability of the Au NPs, i.e., a gradient force, act on the NPs.[39] At the resonant wavelength, the gradient force, which is relatively minor, cannot counteract the scattering force that pushes Au NPs out of the focal area [Text S1 and Fig. S1 of the Supplementary Materials (SM)]. In our investigation, we found that in addition to these forces, the electromagnetic force, amplified by the tip's enhancement effect, substantially influences Au NP trapping. The electric field enhancement factor, defined as $M_{\text{loc}} = (E/E_0)^2$ (E is the local electric field intensity and E_0 is background electric field intensity), can reach up to 2.66×10^3 when an Au NP is close to the tip's apex [1 nm, see Fig. 1(a)]. To thoroughly examine the total optical force exerted on Au NPs, we utilized time-averaged Maxwell stress tensor method (more details in Section 2). Figure 1(b) indicates the force applied by the apex on an Au NP in four different directions. These figures differentiate between positive and negative forces, indicating their direction.

Due to the uncertainty in the tip curvature radius, we calculated the optical forces and electric field enhancement for different curvature radii (6, 8, and 10 nm). Specifically, when an Au NP is positioned along the positive X-axis direction, M_{loc} is maximized, resulting in an optical force directed toward the apex of 0.44 ± 0.08 pN. The apex exerts a pulling force on Au NPs that is effective within a 10 nm range, with a measured force of 0.0075 ± 0.0013 pN at this distance along the X-axis [Fig. 1(c)]. This force diminishes for Au NPs located on the side of the apex, primarily because of the lack of a lightning-rod effect,[40] which results in a weaker optical pulling force compared with Au NPs directly in front of the apex. Au NPs experience a pulling force directed toward the apex even when positioned at a distance [Fig. 1(d)], attributable to both scattering and electromagnetic forces that orient toward the focal point along the positive Z-axis. Figure 1(e) indicates a transition from an optical pulling force to an optical pushing force when the Au NP-apex separation exceeds 3 nm, indicating the predominance of electromagnetic over scattering forces within this distance. Furthermore, figure 1(f) evaluates the optical force dynamics on an Au NP along the positive Y-axis, confirming its capability for near-field trapping in this orientation. We find that the apex generates a pulling force on Au NPs over several nanometers across all directions and the influence of curvature radius is mainly within a range of 1 nm. These results all underscore tip's potential for precise NP trapping. In addition, our method is not only confined to Au NPs but also suitable for numerous nanoparticles with plasmonic effects including metal nanoparticles and some core-shell nanoparticles (Text S2 and Fig. S2 of the SM).

3.2. Tip-Assisted Nanoparticles Capture and Raman Thermometry. To verify the above results, we conducted experiments based on simulations, illustrating the deposition of Au NPs onto the tip and their directed migration toward the conical apex (500 nm in height) along the tip's wall. We used an optical setup [Fig. 2(a)] in conjunction with field-emission scanning electron microscopy (SEM) to evaluate the tip morphologies. The experiments utilized a 532 nm continuous-wave laser to excite the plasmonic resonance of 60 nm diameter Au NPs, which have a surface plasmon resonance peak at approximately 540 nm[41] in water (Text S3 and Fig. S3 of the SM). After conducting the trapping experiments, we removed the tips from the Au NP suspension and imaged them using SEM. To assess the effects of the Au NP suspension and laser illumination on the tip's trapping efficiency, we established two control groups for SEM analysis.

In the first control group, we compared a non-illuminated tip with a pristine, smooth tip (Text S4 and Fig. S4 of the SM). This comparison indicates the presence of water on the tip's surface, which carried Au NPs, likely remnants from the tip's removal. This observation also

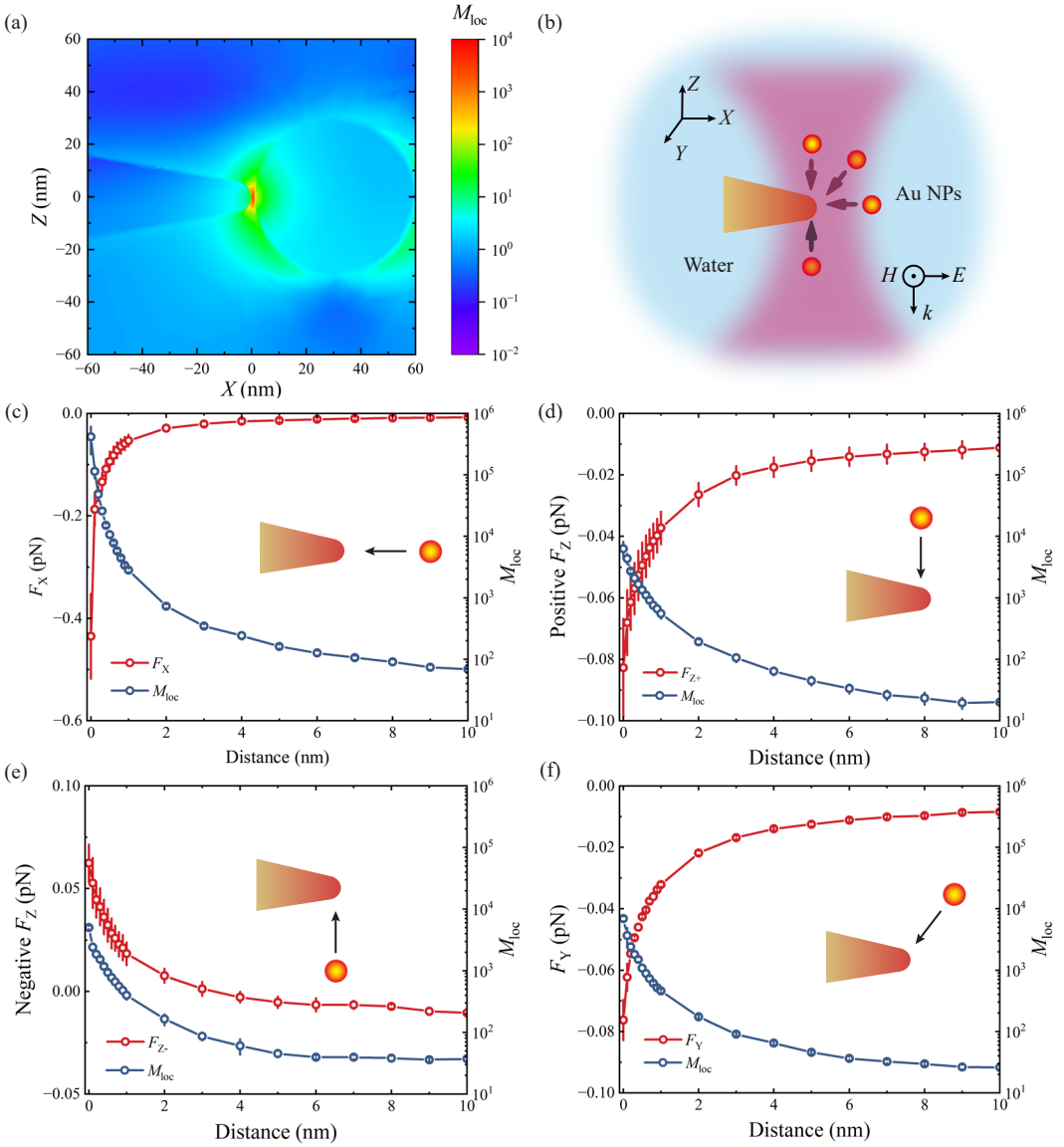

Fig. 1. Directional optical forces induced by tip-enhanced electric field. (a) Front view of the electric field distribution around the tip-NP system (single Au NP in the $X+$ direction) in the $y = 0$ plane. We set the origin at the highest point of the apex in the simulation. (b) Schematic of tip-NP simulation model. Au NPs are scattered around the tip apex. (c)–(f) Directional optical pulling force ($\boldsymbol{F}_o$) of the apex on the Au NP in four directions ($X+$, $Z+$, $Z-$, $Y+$). The incident laser beam follows the Z-axis from top to bottom. The error bars represent the standard deviation of optical forces and electric field enhancement for a tip curvature radius ranging from 6 to 10 nm.

suggests that the Au NPs in suspension were uniformly distributed. The second control group involved a comparison between tips subjected to laser irradiation and those not subjected to it. Areas of the tip exposed to laser light attracted a higher concentration of Au NPs, which formed stripes or clusters, presumably because of mutual collisions among the Au NPs. The top-down SEM analysis of the laser-illuminated tip, along with the SEM image of the illuminated tip after rinsing (Text S5 and Fig. S5 of the SM), confirmed 3D trapping of Au NPs. Interestingly, Au NPs remained on the tip's surface even after we removed the tip from the suspension, indicating that their trapping was irreversible. This outcome is likely due to Au NPs colliding with the tip and overcoming electrostatic repulsion at its surface.[42,43] Note that Au NPs are also present on the surface of the tip, which is attributed to optical forces and thermal convection induced by it during focusing (Text S6 and Fig. S6 of the SM). This irreversible trapping might present a feasible method for preparing specialized tips for use in tip-enhanced Raman spectroscopy (TERS).[44]

To obtain the trapping potential, we performed supplementary experiments (Text S7 and Fig. S7 of the SM) by observing the distribution of Au NPs around the nanotip, as reported by Hong *et al.*[45] The experimental results show that the bright areas around the nanotip increased significantly after 0.5 s, thus demonstrating the trapping of Au NPs by the nanotip. However, the trapping range is limited to the nanoscale, and the camera cannot

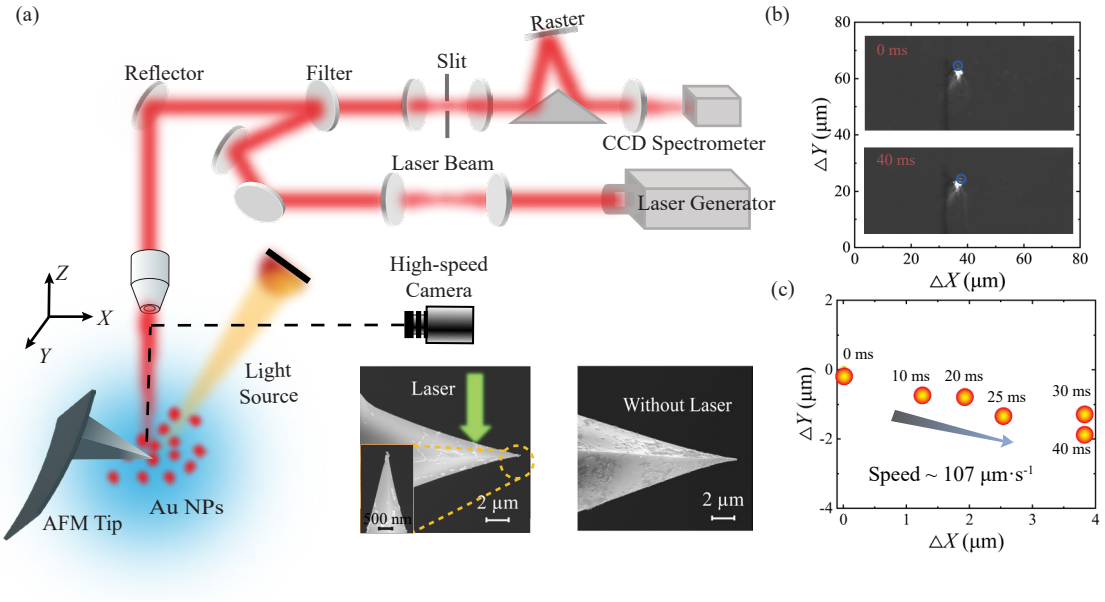

Fig. 2. Schematic of the tip-assisted nanoparticles capture system. (a) Optical alignment for trapping and thermal sensing. Excited Raman signals are received through the same optical path, whereas the incident laser beam at 532 nm focuses on the probe tip apex in a manner that traps Au NPs. Insets show an SEM image of the tip apex with and without the irradiating laser. Trapping is recorded with a high-speed camera through the same objective lens from above. We photographed the tips after the experiment using SEM. (b) Images recorded with a high-speed camera at 0 and 40 ms show Au NPs moving toward the apex. (c) Position of Au NPs from 0 to 40 ms; position is relative to the starting point (0 ms). The average velocity of Au NPs is 106 $\mu m \cdot s^{-1}$.

distinguish the distribution of Au NPs within a range of several nanometers during the experiment, which leads to difficulty in determining the trapping potential using this experimental approach. Therefore, we calculated the trapping potential, shown in Text S8 and Fig. S8 of the SM. The results indicate that the trapping potential realized in this research is higher, demonstrating its highly localized trapping range.

We also evaluated the trajectory of Au NPs near the AFM tip using a high-speed camera (Movie S1 as one of the SM). We achieved localized heating of the tip and surrounding Au NPs by irradiating the tip with a laser at a power intensity of 0.15 $mW \cdot \mu m^{-2}$. This process generates a thermal-osmotic force because of the temperature gradient [46] from the tip's cooler base to its warmer apex, driving Au NPs upward along the tip's side [Fig. 2(b)]. We evaluated the speed of the Au NPs by processing the high-speed camera footage with MATLAB, with their positions over time shown in Fig. 2(c). We determined an average movement speed of approximately 107 $\mu m \cdot s^{-1}$ for Au NPs advancing from the base of the tip to the apex. Notably, the intensity of scattered light from these Au NPs increased during their ascent, signifying their aggregation. This clustering is likely due to collisions among Au NPs moving at varied speeds, which overcome their electrostatic repulsion, [43] leading to substantial aggregation near the tip's apex.

In addition to optical forces, thermophoretic forces (F_{tp}), driven by temperature gradients, play a critical role in hindering nanoparticle trapping, warranting close study in our work. To quantify the temperatures of the AFM tip and Au NPs, we utilized FWHM-based Raman thermometry (more details in Section 2). This approach is based on the known quadratic relationship between the FWHM of silicon and temperature, extending from 0 up to 500 °C. [47,48] A calibration experiment using a standard silicon chip from the AFM tip is conducted to determine the coefficients in Eq. (3). Here, a low excitation laser power of 1 mW is employed to prevent additional heating of the chip. As shown in Fig. S9 of the SM, after precise fitting, the calibration coefficients are obtained as $B = 6 \times 10^{-6}\,cm^{-1} \cdot K^{-2}$, $C = 3.83 \times 10^{-6}\,cm^{-1} \cdot K^{-2}$, $\Gamma_0 = 3.21\,cm^{-1}$. These parameters show good agreement with those from Beechem *et al.*, [48] confirming the credibility of our work. In Fig 3(a), the FWHM at various powers of the nanotip is depicted. Based on this linear relationship in the figure, we aligned the FWHM at 0 mW power with the value of Γ_0. Figure 3(b) shows calculated tip temperatures in air and water under varying laser powers (1.3–6.4 mW). Our findings indicate a notably lower temperature increase in water compared with air, attributable to water's superior thermal conductivity and heat capacity; these results showcase substantial impact on thermal dynamics.

To estimate the temperature field of the apex and Au NPs, we constructed a 3D model based on experimental parameters and conducted simulations using the FEM. The thermal conductivity of silicon at the nanoscale is substantially smaller than the bulk value because of strong ballistic heat transfer. [49] This can be qualitatively verified by noting that the temperature increase coefficient of the nanotip (48.17 $K \cdot m \cdot W^{-1}$) is higher than that of bulk silicon (1.42 $K \cdot m \cdot W^{-1}$) [50] in air. Thus, the local thermal

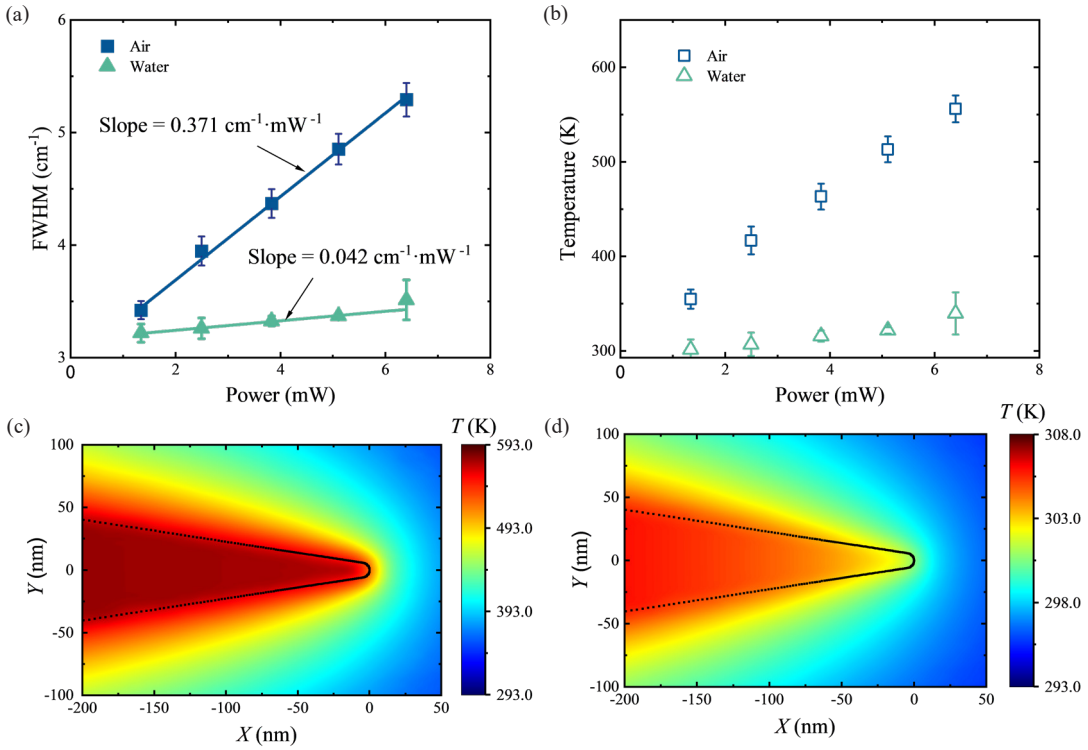

Fig. 3. Temperature analysis of the apex. (a) The changes in nanotip FWHM under different incident laser powers (1.3–6.4 mW), with slopes of 0.371 $cm^{-1}\cdot K^{-1}$ and 0.042 $cm^{-1}\cdot K^{-1}$ in air and water. The measured Raman spectrum is shown in Text S10 and Fig. S10 of the SM. (b) Temperatures of the same tip in air and water at various powers of laser beam irradiation. Simulated temperature of the apex in (c) air and (d) water medium ($y = 0$ plane). The temperatures of the apex in air and water are 570 K and 302 K, respectively.

conductivity (k_{eff}) of the silicon tip can be expressed as $k_{\text{eff}} = [3k/(3 + 4/\tau)]$; where k is the thermal conductivity of bulk silicon, and τ is the dimensionless radial distance, which can be expressed as r/Λ. Λ is set as 43 nm in simulation for mean free path of phonons in bulk material.[51] The temperatures of the apex in air and water are 570 K and 302 K, respectively [Fig. 3(c)]. The absolute errors between simulated and experimental values in air and water are less than 5%, affirming the applicability of local thermal conductivity in this study.

3.3. Analysis of Thermophoretic Force and Interatomic Force. The thermal effects in the nanotip have been evaluated and will influence the trapping of Au NPs, as reported in recent work.[52,53] Here, we simulated a typical situation in which an Au NP is in contact with the apex to evaluate the influence of thermophoresis. Analyzing the temperature field in Fig. 4(a), we inferred that the temperature of the Au NP is slightly higher (~ 2 K) than that of the apex in contact mode, attributable to enhanced plasmonic heating by the tip. By comparing the simulated temperatures of the apex in water and Au NP suspension, we found that the temperature in the Au NP suspension was 3 K higher than that in water, which is consistent with changes observed in Raman spectrum during experiments (Text S11 and Fig. S11 of the SM). Thus, the enhancement effect between the tip and Au NPs corresponds to higher temperature increases for the tip.[54]

The temperature distribution analysis enabled the calculation of both the average temperature gradient (ΔT_{gra}) and the thermophoretic velocity of an Au NP at varying distances [Figs. 4(b) and 4(c)]. The thermophoretic velocity V_{tp} is described as $V_{\text{tp}} = -D_{\text{T}}\Delta T$, where D_{T} is thermophoretic mobility, usually in a range of 1–10 $\mu m^2\cdot s^{-1}\cdot K^{-1}$ in experiments.[55,56] In the calculation, D_{T} is assumed to be 5 $\mu m^2\cdot s^{-1}\cdot K^{-1}$. The closer this is to the apex, the lower the ΔTgra and V_{tp} of the Au NPs; this indicates that the apex weakens the original thermophoretic force on the Au NP because of the temperature difference between the Au NP and apex. Through V_{tp} obtained, the thermophoretic force can be calculated with $F_{\text{tp}} = 3\pi d\eta V_{\text{tp}}$. In this equation, d is the diameter of the Au NP (60 nm), $\eta = 6.81 \times 10^{-4}$ Pa·s is the viscosity of water at a temperature of 306 K. Figure 4(d) indicates that net force F_{net} acting on an Au NP—dependent on F_{tp} and optical force F_{o}—is always positive; indicating that the Au NP will be pushed away from apex by F_{tp}. Regarding F_{net}, the Au NPs are still subjected to a pulling force toward apex within a range of 2 nm after taking into account thermophoretic force. Hence, the apex still exerts a strong pulling force on Au NPs within a range of several nanometers even with presence of thermophoretic force.

Here, in such a trapping range, interatomic forces will become important. To further validate our findings, we also conducted a large-scale all-atom molecular dynamics simulation ($\sim$five million atoms) using large-scale atomic/molecular massively parallel simulator with

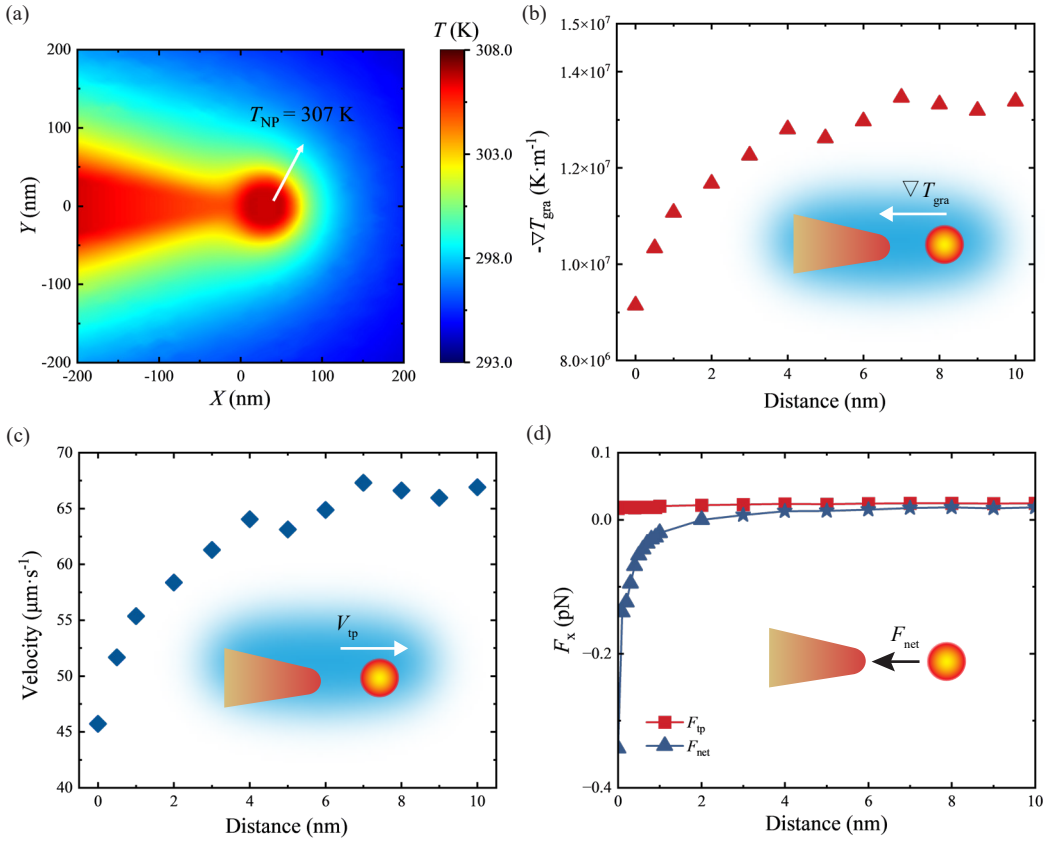

Fig. 4. Analysis of thermophoresis force and net force acting on the Au NP. (a) Temperature of the apex and Au NP in contact mode. The power of the incident laser beam is 6.4 mW, corresponding to the experimental value. (b) ΔT_{gra} and (c) velocity of Au NP. The thermophoresis force decreases with increasing distance. (d) F_{tp} and net force F_{net} of the Au NP in the $X+$ direction at various distances (0–10 nm). The Au NPs are still subjected to a pulling force toward the apex within a range of ~ 2 nm after taking into account the thermophoresis force.

realistic water, Au NP, and silicon nanotip models (Text S12 and Fig. S12 of the SM). The results suggest that interatomic forces, such as van der Waals forces or repulsive forces, are dominant when the two bodies are very close (around 5 Å). These forces could easily overwhelm the maximum optical force (which is on the order of 0.35 pN), making interatomic forces the dominant factor within this short range. However, for the range of 12 Å to 15 Å, the interaction between the silicon nanotip and Au NP is much weaker compared to the forces at shorter distances. In this distance range, optical forces (which are approximately 0.35 pN as stated) become comparable to or stronger than the interaction forces, allowing for effective trapping of the nanoparticle. Additionally, we have conducted molecular dynamics simulations to show the natural diffusion and trapping process (Text S13, Fig. S13 and Movie S2). These results indicate that the Au NP immersed in realistic water will be trapped onto the silicon nanotip. This observation is consistent with previously established trapping phenomena, providing additional support for our results.

4. Conclusions. This study demonstrates an efficient tip-assisted nanoparticle capture system utilizing the substantial electric field enhancement between an AFM tip and Au NPs at a reduced laser power density of 0.15 mW·μm^{-2}, achieving a 42% reduction compared with previous methods for trapping Au NPs of similar size. We observed Au NPs propelled from the base toward the tip's apex at a velocity of 107 μm·s^{-1}, driven by a thermal-osmotic force. Near the apex, a strong electromagnetic force pulls the Au NPs within the range of a few nanometers despite thermal effects. Notably, Au NPs remain on the tip's surface after the experiments, and the enhanced Raman scattering of the tip-Au NPs is experimentally confirmed, suggesting a method for creating specialized tips for TERS research. Considering the substantial decrease in local thermal conductivity at the nanoscale compared with bulk materials, we also validate our calculations of effective thermal conductivity (k_{eff}) for nanotips through experiments and simulations. Furthermore, thermal simulations suggest that the AFM tip decorated with Au NPs enhances localized plasmonic heating, potentially facilitating controllable generation of micro/nano bubbles on the tip at low laser power.

Overall, this approach not only mitigates thermal effects in nanoparticle trapping but also advances high-resolution TERS technology for micro/nanoscale thermal analysis,[26] biosensing,[57] and materials characterization.[58] Furthermore, we expect the aforementioned tip-induced bubble generation to play a major role in lab-on-a-chip systems, micro/nano plastic detection, and energy-

efficient applications.[59]

Acknowledgements. We are grateful to the members of the Advanced Thermal Management & Energy Storage Lab for helpful discussion. This work was supported by the National Natural Science Foundation of China (Grant No. 52206107) and the National Key R&D Program of China (Grant No. 2023YFE0120200). The simulations were supported by the Research Computing Center in Wuhan University.

References

[1] Polimeno P, Magazzu A, Iati M A, Patti F, Saija R, Boschi C D E, Donato M G, Gucciardi P G, Jones P H, and Volpe G 2018 *J. Quant. Spectrosc. Radiat. Transf.* **218** 131
[2] Pesce G, Jones P H, Maragò O M, and Volpe G 2020 *Eur. Phys. J. Plus* **135** 949
[3] Xin H, Li Y, Liu Y C, Zhang Y, Xiao Y F, and Li B 2020 *Adv. Mater.* **32** 2001994
[4] Bustamante C J, Chemla Y R, Liu S, and Wang M D 2021 *Nat. Rev. Methods Primer* **1** 25
[5] Zhu R, Avsievich T, Popov A, and Meglinski I 2020 *Cells* **9** 545
[6] Chen J, Chen Z, Meng C, Zhou J, Peng Y, Dai X, Li J, Zhong Y, Chen X, and Yuan W 2023 *Light Sci. Appl.* **12** 273
[7] Chen J, Zhou J, Peng Y, Dai X, Tan Y, Zhong Y, Li T, Zou Y, Hu R, and Cui X 2024 *Adv. Mater.* **36** 2309143
[8] Eechampati A and de Silva C 2022 *Appl. Nano* **3** 43
[9] Hong C, Yang S, and Ndukaife J C 2020 *Nat. Nanotechnol.* **15** 908
[10] Ruttley D K, Guttridge A, Spence S, Bird R C, Le Sueur C R, Hutson J M, and Cornish S L 2023 *Phys. Rev. Lett.* **130** 223401
[11] Mazzanti M, Schüssler R X, Espinoza J A, Wu Z, Gerritsma R, and Safavi-Naini A 2021 *Phys. Rev. Lett.* **127** 260502
[12] Teoh Y H, Sajjan M, Sun Z, Rajabi F, and Islam R 2021 *Phys. Rev. A* **104** 022420
[13] Kolbow J D, Lindquist N C, Ertsgaard C T, Yoo D, and Oh S H 2021 *Chem. Phys. Chem.* **22** 1409
[14] Sun W, Gao X, Lei H, Wang W, and Cao Y 2022 *Adv. Sci.* **9** 2105254
[15] Sarshar M, Wong W T, and Anvari B 2014 *J. Biomed. Opt.* **19** 115001
[16] Hansen P M, Bhatia V K, Harrit N, and Oddershede L 2005 *Nano Lett.* **5** 1937
[17] Ren Y, Chen Q, He M, Zhang X, Qi H, and Yan Y 2021 *ACS Nano* **15** 6105
[18] Koya A N, Cunha J, Guo T L, Toma A, Garoli D, Wang T, Juodkazis S, Cojoc D, and Proietti Zaccaria R 2020 *Adv. Opt. Mater.* **8** 1901481
[19] Ma J, Zhang H, Lou Y, Min Q, Wu D, Wang Y, and Pang Y 2024 *Nano Lett.* **24** 12605
[20] Novotny L, Bian R X, and Xie X S 1997 *Phys. Rev. Lett.* **79** 645
[21] Mestres P, Berthelot J, Aćimović S S, and Quidant R 2016 *Light Sci. Appl.* **5** e16092
[22] Chen G 1996 *J. Heat Transfer* **118** 3
[23] Lehmuskero A, Johansson P, Rubinsztein-Dunlop H, Tong L, and Kall M 2015 *ACS Nano* **9** 3453
[24] Guo G, Feng T, and Xu Y 2018 *Opt. Lett.* **43** 4961
[25] Li M, Li C, Wang J, Xiao X, and Yue Y 2015 *Appl. Phys. Lett.* **106** 25
[26] Huang D, Sun Q, Liu Z, Xu S, Yang R, and Yue Y 2023 *Adv. Sci.* **10** 2204777
[27] Wang R, Xu S, Yue Y, and Wang X 2020 *Int. J. Extreme Manuf.* **2** 032004
[28] Deng S, Xu S, Gao J, Wu H, She J, and Yue Y 2022 *J. Phys. Chem. C* **126** 1922
[29] De Wolf I 1996 *Semicond. Sci. Technol.* **11** 139
[30] Mark P and Nilsson L 2001 *Phys. Chem. A* **105** 9954
[31] Huang D, Ma R, Zhang T, and Luo T 2018 *Appl. Mater. Interfaces* **10** 28159
[32] Huang D, Zhang T, Xiong G, Xu L, Qu Z, Lee E, and Luo T 2019 *Appl. Mater. Interfaces* **11** 32481
[33] Luo T and Lloyd J R 2010 *J. Heat Transfer* **12** 3
[34] Sierra-Suarez J A, Majumdar S, McGaughey A J, Malen J A, and Higgs C F 2016 *J. Appl. Phys.* **119** 145306
[35] Luo T and Lloyd J R 2010 *Int. J. Heat Mass Transf.* **53** 1
[36] Jaeger R, Lagowski J B, Manners I, and Vancso G J 1995 *Macromolecules* **28** 539
[37] Chen W, Zhang J, and Yue Y 2016 *Int. J. Heat Mass Transf.* **103** 1058
[38] Zhang T, Gans-Forrest A R, Lee E, Zhang X, Qu C, Pang Y, Sun F, and Luo T 2016 *Appl. Mater. Interfaces* **8** 33326
[39] Wang S and Ding T 2019 *ACS Nano* **13** 32
[40] Zeng Z, Quan X, Yu H, Chen S, and Zhang S 2019 *J. Catal.* **375** 361
[41] Semwal V, Jensen O R, Bang O, and Janting J 2023 *Micromachines* **14** 1717
[42] Zhou J, Ralston J, Sedev R, and Beattie D A 2009 *J. Colloid Interface Sci.* **331** 251
[43] Aldewachi H, Chalati T, Woodroofe M N, Bricklebank N, Sharrack B, and Gardiner P 2018 *Nanoscale* **10** 18
[44] Cao Y and Sun M 2022 *Rev. Phys.* **8** 100067
[45] Hong C, Hong I, Jiang Y, and Ndukaife J C 2024 *Adv. Opt. Mater.* **12** 2302603
[46] Zhou J, Dai X, Peng Y, Zhong Y, Ho H-P, Shao Y, Gao B Z, Qu J, and Chen J 2023 *Nano Res.* **16** 7710
[47] Huang X, Wang Y, Deng S, and Yue Y 2023 *Int. J. Heat Mass Transf.* **209** 124124
[48] Beechem T, Graham S, Kearney S P, Phinney L M, and Serrano J R 2007 *Rev. Sci. Instrum.* **78** 061301
[49] Yue Y, Liu K, Li M, and Hu X 2014 *Carbon* **77** 973
[50] Lubio A D, Dörfler A, Plathier J, Dequivre T, Kolhatkar G, Charlebois S A, and Ruediger A 2021 *J. Raman Spectrosc.* **52** 1123
[51] Liu W and Asheghi M 2006 *J. Heat Transfer* **128** 75
[52] Jiang Q, Rogez B, Claude J-B, Baffou G, and Wenger J 2020 *Nano Lett.* **20** 8811
[53] Anyika T, Hong I, Zhu G, and Ndukaife J C 2025 *Laser Photonics Rev.* **19** 2400412
[54] Rigor J, Kurouski D, and Large N 2022 *J. Phys. Chem. C* **126** 13986
[55] Piazza R 2008 *Soft Matter* **4** 1740
[56] Setoura K, Tsuji T, Ito S, Kawano S, and Miyasaka H 2019 *Nanoscale* **11** 21093
[57] Safar W, Azziz A, Edely M, and Lamy de la Chapelle M 2023 *Chemosensors* **11** 399
[58] Bao Y F, Zhu M Y, Zhao X J, Chen H X, Wang X, and Ren B 2024 *Chem. Soc. Rev.* **53** 10044
[59] Liu X, Yang J, Zou Q, Hu Y, Li P, Tan L, Miljkovic N, and Yang R 2025 *ACS Nano* **19** 9513